

# A global radio frequency noise survey as observed by the FORTE satellite at 800 km altitude

Tom Burr

Statistical Sciences Group, Los Alamos National Laboratory, Los Alamos, New Mexico, USA

Abram Jacobson

Space and Atmospheric Sciences Group, Los Alamos National Laboratory, Los Alamos, New Mexico, USA

Angela Mielke

Space Data Systems, Los Alamos National Laboratory, Los Alamos, New Mexico, USA

Received 23 December 2002; revised 11 May 2004; accepted 27 May 2004; published 24 July 2004.

[1] We present a global radio frequency noise survey observed from the Fast on-Orbit Recording of Transient Events (FORTE) satellite at 800 km altitude. This is a survey of squared amplitudes ( $R^2$ ) in 44 frequency subbands spaced by 0.5 MHz centered at 38 MHz (“low band”) and 44 subbands spaced by 0.5 MHz centered at 130 MHz (“high band”). We define 13 geographic regions and analyze signal-free regions of event data, generated from November 1997 to December 1999, that we assume are representative of the noise of interest (discussion provided). Because this noise distribution is nonstationary, we use cross validation to sample the distribution across time. Summary statistics presented for  $R^2$  include the mean, median, percentiles, and fractions exceeding thresholds in each of the 44 subbands for the low- and high-frequency bands in each of the geographic regions. Fractions exceeding thresholds are particularly relevant to multiband signal detection. In the low band the  $R^2$  versus frequency plot for each of the 13 regions has peaks in the mean and median at approximately 35 MHz; many regions have peaks at approximately 28 and 45 MHz. The high-band spectral plots are generally slightly smoother with less dramatic peaks than in the low band. The values of  $10 \times \log_{10}(R^2)$  range from approximately  $-110$  to  $-70$  for both the low band and high band and are generally slightly larger in the low band. The continental United States (CONUS) region low band is notably higher, with values ranging from  $-105$  to  $-62$ . Several future satellite projects involving triggered radio frequency broadband signal recordings can benefit from a realistic trigger-noise survey such as done here. *INDEX TERMS:* 1204

Geodesy and Gravity: Control surveys; *KEYWORDS:* global, noise, survey

**Citation:** Burr, T., A. Jacobson, and A. Mielke (2004), A global radio frequency noise survey as observed by the FORTE satellite at 800 km altitude, *Radio Sci.*, 39, RS4005, doi:10.1029/2002RS002865.

## 1. Introduction

[2] Space-based observations of radio frequency (RF) emissions have several applications, including lightning RF signatures, nuclear weapon detection, long-baseline radio astronomy, and an exciting area of cosmic ray research involving an unknown source of highly ener-

getic primary particles [Jacobson *et al.*, 1999]. In order to detect such signals, it is necessary to quantify aspects of the background such as intensity, spectral features, and the timescales over which both change.

[3] The Fast on-Orbit Recording of Transient Events (FORTE) [Jacobson *et al.*, 1999] satellite records very high frequency (VHF) RF observations in a low (centered at 38 MHz) and high (centered at 130 MHz) band receiver. RF emissions that satisfy a multiband trigger criterion are archived, and these “event records” include presignal and postsignal regions that remain available to

This paper is not subject to U.S. copyright.

Published in 2004 by the American Geophysical Union.

evaluate. We assume that these signal-free regions provide a representative sample of the RF noise (see section 3) and provide an RF noise survey by evaluating these regions of the event records.

[4] Several future satellite projects involving triggered RF broadband signal recordings can benefit from a realistic trigger-noise survey such as done here. One such beneficiary is the search for cosmic-ray-shower RF emissions [Lehtinen *et al.*, 2004]. Another application is satellite-based long-baseline radio astronomy. We use simple thresholding to extract the signal and then analyze the two remaining signal-free regions.

[5] Our noise survey is a “static” survey of amplitudes at each of 44 subbands spaced by 0.5 MHz (from 26.5 to 48 MHz in the low band and from 118.5 to 140 MHz in the high band). Appendix A provides more detail about our spectral analysis approach. Briefly, any sequence of  $n$  numbers  $X_1, X_2, \dots, X_n$  has the Fourier series representation (we assume that  $n$  is even for convenience):  $X_t = a_0 + \sum_{p=1}^{n/2-1} \{a_p \cos(2\pi p t/n)\} + b_p \sin(2\pi p t/n)$ , which, for  $p \neq n/2$ , is equivalent to  $X_t = a_0 + \sum_{p=1}^{n/2-1} R_p \cos(\omega_p t + \phi_p)$  with the phase  $\phi_p = \tan^{-1}(-b_p/a_p)$ .

[6] In our case the raw data  $X$  are the electric field  $E$  in V/m at the satellite. We refer to  $R_p$  as the amplitude at frequency  $p$ . Like the electric field  $E$ ,  $R_p$  is in units of V/m. In this paper we report smoothed estimates of  $R_p^2$  using a 1 MHz wide smoother, and for graphing purposes, we usually use the decibel scale (dB) and plot  $10 \times \log_{10}(R_p^2)$ . Throughout this paper,  $R_p$  will refer to either the estimated or true amplitude at frequency  $\omega_p$ , and the meaning will be clear from context.

## 2. Other Radio Frequency Noise Surveys

[7] Kaiser *et al.* [1996] surveyed RF noise from 1 to 14 MHz, using data from the Wind satellite collected approximately 200,000 km above Earth, and provided evidence for local temporal and also geographic patterns, mostly explained by the satellite’s changing field of view. Another space-based RF survey at 1.0–5.6 MHz measured from 100,000 to 120,000 km above Earth is reported in the work of LaBelle *et al.* [1989], which also reviews other RF noise and signal surveys. However, none of these consider the frequency ranges presented here. LaBelle *et al.* [1989] find important differences in 1.0–5.6 MHz RF emissions depending on whether intense auroral kilometric radiation is present. They also find noise bursts with patterns such as larger amplitude when the satellite is nearer to Earth and zero bursts when the satellite is within 4 hours of local noon, with bursts sporadically present at other times. In the work of LaBelle *et al.* [1989, Figure 2], there is obvious nonstationarity over the 1 year review period. In the work of LaBelle *et al.* [1989, Figures 4 and 5], there is obvious nonstationarity over the 5–7 hour period. In addition, in

the work of LaBelle *et al.* [1989, Figure 6, p. 735], there is qualitative evidence that “on the timescale of seconds, the background level is constant except for fluctuations of the order of 10%.” The noise details differ depending on whether intense auroral kilometric radiation is present, but qualitatively, the noise exhibits long-term drifting and bursting, which are two types of nonstationarity. Certainly some of the drifting is due to field of view changes as with FORTE.

[8] Other RF surveys are reviewed in the handbook edited by Volland [1995]. Again, none of these surveys consider the FORTE frequency range. Chapter 12 (“Low-frequency radio noise”) includes tutorial detail regarding, e.g., “voltage deviation,” and amplitude probability distributions. The voltage deviation  $V_d$  measures the impulsiveness or “spikiness” of noise and is more relevant if, e.g., we use moving averages to mitigate the impact of a changing mean value. The amplitude probability distribution is also more relevant to the case when moving averages of the recent background are used, especially regarding percentiles of the noise distribution. Chapter 13 (“Radio noise above 300 kHz due to natural causes”) reviews noise sources and typical energy spectra (energy spectral density versus frequency such as in some of our figures). It also describes spectral analysis methods and methods to infer aspects of the RF source using intensities, polarization, spectra, and facts regarding propagation of radio waves. Chapter 14 reviews atmospheric noise and its effects on telecommunication performance and includes estimates of the maximum and minimum environmental noise factors as we provide below for the FORTE frequency range.

[9] LaBelle *et al.* [1989] also compared noise amplitudes with a previous survey [Herman *et al.*, 1973] and found evidence of increasing man-made terrestrial background between 1973 and 1988. In our case we have found no statistically significant change over the review period of November 1997 to December 1999.

## 3. FORTE Satellite

[10] On 29 August 1997, FORTE was launched as a joint experiment between Los Alamos National Laboratory and Sandia National Laboratory. The goal has been to provide advanced RF impulse detection and characterization. FORTE was launched into a nearly circular low-Earth orbit at an approximate altitude of 800 km and 70 degree inclination. The emphasis of this satellite is on the measurement of electromagnetic pulses, primarily due to lightning, within a noise environment dominated by continuous wave carriers, such as TV and FM stations (nis-www.lanl.gov/nis-projects/forte\_science). The FORTE payload consists of three measurement instruments: an RF system, an optical system, and an

**Table 1.** Latitude and Longitude Definition of Each of the 13 Regions

Region	Longitude	Latitude
Africa	20	−10
Australasia	130	−30
Central America	−90	10
CONUS	−100	40
Indian Ocean	70	−30
North Atlantic	−40	40
NE Pacific	−160	30
NW Pacific	160	40
South America	−60	−30
South Atlantic	−10	−40
Southeast Asia	100	20
SE Pacific	−160	−30
SW Pacific	160	−40

“event classifier.” These systems have previously been described in detail [Jacobson *et al.*, 1999]. For convenience we will briefly describe the RF system here.

[11] The RF system is designed to receive, digitize, store, and down-link records of interest. These records contain VHF time series of the RF electric field,  $E$ , digitized at a rate of 50 megasamples/s [Jacobson, 2003]. Typically data are collected in passband regions (low and high). When a multiband trigger criterion is met, typically twelve-bit data are collected from one or both of these passbands for a period of 409.6  $\mu$ s, although event records exist with a collection period of two and four times this duration. One quarter of the collected waveform is produced from the pretrigger, and because the events are usually very short, nearly three quarters of the waveform is from the posttrigger.

[12] Each RF passband receiver has embedded within it eight independent triggering subbands spaced at 2.5 MHz with 1 MHz bandwidths. The two 22 MHz receivers are triggered together enabling both to be digitized synchronously. The trigger rule requires coincidence (within 162  $\mu$ s for the low band and within 10  $\mu$ s for the high band) of typically five (or more) of

the eight subband triggers. Triggering is usually produced by the low band. Each 1 MHz trigger subband has a noise compensation option in which the threshold may be either set at an absolute level or as a value above a low-pass filtered noise level in that subband (i.e., as a noise riding threshold). Normally the signal is required to rise to at least a threshold  $T$  ( $T$  is typically 14–20 dB) above the background noise in order to trigger a given subband, which means that  $10 \times \log_{10}(R^2/R_{\text{background}}^2)$  must be at least  $T$  for the subband to alarm. The alarm rate of this rule on noise of the type considered in this survey has not been formally evaluated, although it is evident that this type of rule triggers on many lightning events while maintaining a very low false alarm rate on the noise considered here. However, as we will show, the noise can vary by 20 dB between the quietest and the noisiest portions of Earth.

#### 4. Data Selection and Preprocessing

[13] The RF receiver on the FORTE satellite has collected several hundred thousand transionospheric pulse pair (TIPP) events from November 1997 to December 1999. These TIPP events are defined as VHF signals consisting of two broadband pulses, each with a duration of a few microns [Tierney *et al.*, 2002] and a characteristic shape. TIPP events are generally associated with thunderstorms and therefore result in several recorded events in a particular Earth region during a single satellite pass over that region. TIPP events typically exhibit a separation of at least several meters (see below). Therefore this noise survey will rely on raw data (the electric field  $E$  in volts per meter) in the form of a time series of signal-free regions from each event, with gaps of a few meters or more between event records that are each usually 409.6  $\mu$ s in duration (a few are 819.2 or 1638.4  $\mu$ s in duration).

[14] As mentioned in the introduction, RF emissions that satisfy a multiband trigger criterion are archived, and these “event records” include presignal and post-

**Table 2.** Correlation Matrix for  $R^2$  at Each of Eight Frequencies Spaced by 2.5 MHz Based on 40,000 Randomly Chosen 10  $\mu$ s Time Windows From the Indian Ocean Region

Frequency, MHz	121 MHz	123.5 MHz	126 MHz	128.5 MHz	131 MHz	133.5 MHz	136 MHz	138.5 MHz
121	1.0	0.91	0.81	0.62	0.67	0.85	0.76	0.28
123.5	0.91	1.0	0.72	0.57	0.64	0.86	0.80	0.31
126	0.81	0.72	1.0	0.58	0.55	0.71	0.64	0.29
128.5	0.62	0.57	0.58	1.0	0.50	0.65	0.48	0.32
131	0.67	0.64	0.55	0.50	1.0	0.76	0.62	0.21
133.5	0.85	0.86	0.71	0.65	0.76	1.0	0.82	0.34
136	0.76	0.80	0.64	0.48	0.62	0.82	1.0	0.31
138.5	0.28	0.31	0.29	0.32	0.21	0.34	0.31	1.0

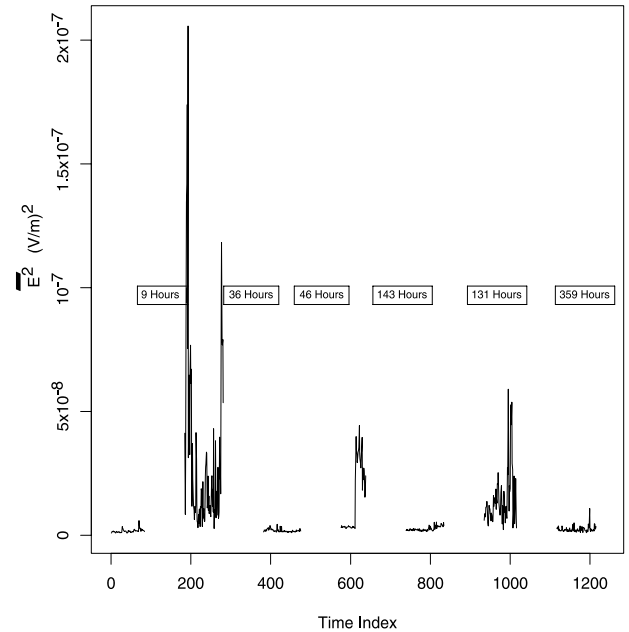
**Table 3.** Correlation Matrix for  $R^2$  at Each of Eight Frequencies Spaced by 2.5 MHz Based on 40,000 Randomly Chosen 10  $\mu$ s Time Windows From the Central America Region

Frequency, MHz	121 MHz	123.5 MHz	126 MHz	128.5 MHz	131 MHz	133.5 MHz	136 MHz	138.5 MHz
121	1.0	0.81	0.38	0.54	0.59	0.72	0.55	0.50
123.5	0.81	1.0	0.62	0.54	0.52	0.70	0.49	0.44
126	0.38	0.62	1.0	0.31	0.23	0.35	0.24	0.21
128.5	0.54	0.54	0.31	1.0	0.39	0.58	0.41	0.34
131	0.59	0.52	0.23	0.39	1.0	0.57	0.39	0.37
133.5	0.72	0.70	0.35	0.58	0.57	1.0	0.62	0.48
136	0.55	0.49	0.24	0.41	0.39	0.62	1.0	0.57
138.5	0.50	0.44	0.21	0.34	0.37	0.48	0.57	1.0

signal regions that remain available to evaluate. Arguably, it would be preferable to gather noise records that were saved according to a random or periodic archiving rule, without triggering on signals because of the possibility of biased sampling. Unfortunately, such FORTE records are not available; however, the use of TIPP as a trigger source for records that otherwise provide “background noise” has been shown to be justified by the tendency of TIPP to be temporally isolated. TIPP having the power and signal-to-noise ratio used in this study almost always occur with several meters or more of separation from any other lightning radio frequency emissions [Jacobson and Light, 2003; Jacobson, 2003; Light and Jacobson, 2002; Jacobson et al., 1999]. Because the FORTE radio frequency record is only 409.6  $\mu$ s, it follows that the portion of the record excluding the TIPP itself is a good sample of the background noise level. If there is a bias associated with sampling the noise from the signal-free region of event records, most likely the bias would be toward noisier than typical. However, apart from the impulsive signals from lightning, we do not generally expect the steady noise background to be enhanced by thunderstorm electrification. Rather, we find that the noise background is dominated by man-made radio emissions. In view of these facts we believe it is safe to assume that the signal-free regions of TIPP events provide a representative sample of the RF noise.

[15] For this survey only TIPP events collected by FORTE’s RF receivers within the low- and high-frequency ranges are considered. We use thresholding to extract the very-short-in-duration signal (any value that exceeds five times the median value in the entire record is considered a signal) and then analyze the two remaining signal-free regions (one presignal region lasting approximately 100  $\mu$ s and one postsignal of region lasting approximately 300  $\mu$ s in the 409.6  $\mu$ s records). Concerning the “5X the median value rule” for finding the signal region, note that the background noise during a FORTE pass over a given geographical region tends to be nearly constant. The noise varies slowly and smoothly as FORTE transits its orbit. FORTE is at 800 km altitude and views a huge patch of Earth. This

patch is circular with >6000 km diameter. At any time, there tends to be many noise sources in the field of view, so that the noise available to FORTE varies slowly as different regions (with different population density, degree of industrial activity, etc.) come above and fall below the radio horizon. However, the power of a TIPP varies randomly, with an overall power<sup>-1</sup> dependence [Jacobson and Light, 2003; Jacobson, 2003]. We select from this random distribution of lightning pulses only those which rise to greater than five times the median within the record. We use the median, not the mean, so that the lightning TIPP pulse itself (occupying less than 20  $\mu$ s, compared to 409.6  $\mu$ s for the total record)

**Figure 1a.** Nonstationarity of raw data. This is a plot of  $E^2$  ( $V/m$ )<sup>2</sup> in each of many 10  $\mu$ s windows (the average is based on 500 values per window) for each of several 15-min passes. Each pass is spaced by several days.

essentially plays no role in determining the “noise” because the median is almost fully determined by the 95% of the record that is pure noise, uncontaminated by TIPP signal.

[16] All events are then grouped into 1 of 13 bins describing their position on Earth on the basis of recorded latitude and longitude. If the closest ground coordinate (listed in Table 1) is within 5000 km of the satellite data point, the event is classified as belonging to the specified Earth region. The events are further classified by regional pass where all events in a particular pass are classified as belonging to the same region and all occur within approximately a 15-min time window. Generally, the South Atlantic region is quiet, so very few TIPP events are recorded there, and the satellite down-link occurs in the NE Pacific region, resulting in few TIPP events being recorded for that region.

## 5. Static Noise Survey

[17] This paper extends the work of *Jacobson et al.* [1999] by extracting the signal-free region of each event record for each of 13 geographic regions as described in section 3. In this section we illustrate that the noise distribution is nonstationary, introduce a cross-validation (CV) scheme to assess our confidence in estimates of several features (such as the median and other percent-

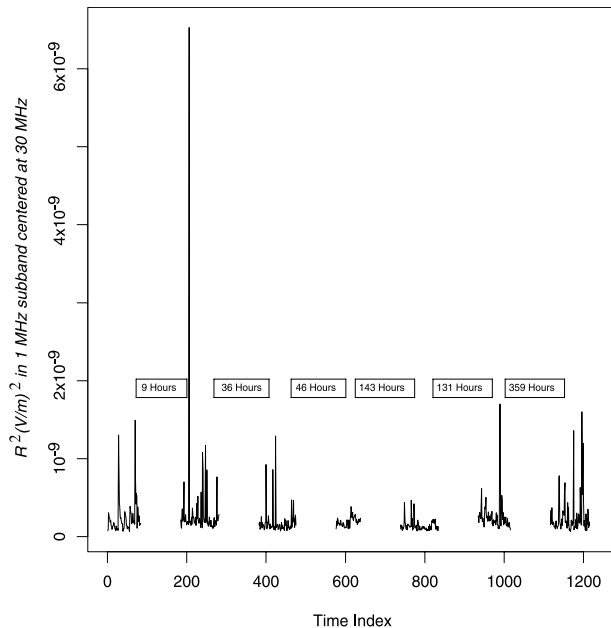


**Figure 1b.** Nonstationarity illustration: same as Figure 1a, except we plot  $R^2$  in a 1 MHz wide subband centered at 30 MHz from each of many 10  $\mu$ s windows to illustrate the nonstationarity.

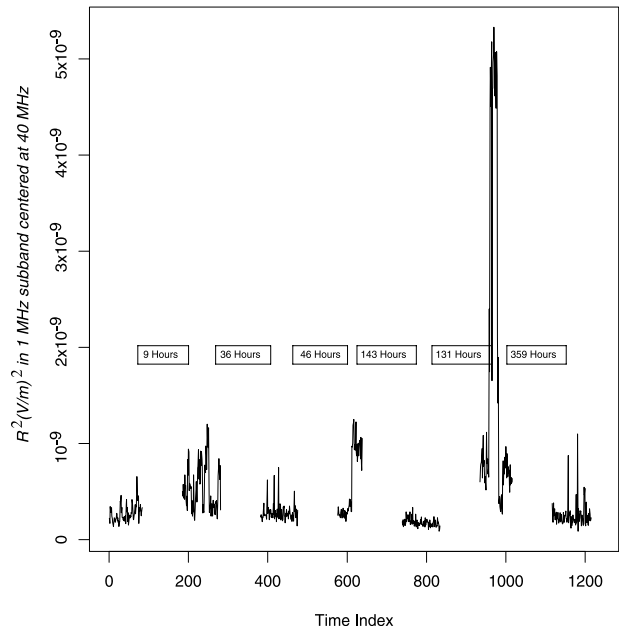


**Figure 1c.** Nonstationarity illustration: same as Figure 1a, except we plot  $R^2$  in a 1 MHz wide subband centered at 40 MHz from each of many 10  $\mu$ s windows to illustrate the nonstationarity.

iles) of the nonstationary noise distribution, describe our spectral analysis approach, and describe the summary statistics we have archived for each region.

### 5.1. Evidence of Nonstationarity

[18] Exploratory analyses (informal graphs and formal statistical tests) suggest that the noise distribution is nonstationary (not constant over time). For example, if the noise were stationary, we would expect zero correlation among the squared amplitudes  $R^2$  (estimated using a 1 MHz bandwidth smoother) in each of a few thousand 10  $\mu$ s windows at 8 frequency bands spaced by 2.5 MHz or more. However, as an example, the correlation matrix for the  $R^2$  at each of 8 frequencies spaced by 2.5 MHz calculated from 40,000 randomly selected times from the Indian Ocean region is given in Table 2. The entries in Table 2 are highly statistically significant because the estimated correlation between nonoverlapping channels (such as those spaced by 2.5 MHz when a 1 MHz bandwidth is used) in a random noise input of length 40,000 varies mostly between  $\pm 0.01$ . Similarly, for the other regions, the correlations that should be nearly zero are instead quite high, sometimes nearly 1 (highly statistically different from 0).

[19] To ensure that this observed correlation is not an artifact of our smoothing (it should not be), we tested our spectral smoother (which has a 1 MHz bandwidth) on



simulated noise and on simulated pure-component inputs both with and without noise. In all the pure noise cases we observed zero (statistically zero) correlation among estimated  $R^2$  in channels spaced by 2.5 MHz or more, as expected. In pure-component inputs at frequency  $\omega_p$  without noise, there is no leakage into frequencies spaced by 2.5 MHz or more from  $\omega_p$ . In pure-component inputs at frequency  $\omega_p$  with noise, whether there is leakage into frequencies spaced by 2.5 MHz or more from  $\omega_p$  depends on the signal-to-noise ratio. Also, because of smoothing with a 1 MHz bandwidth, in all our simulated cases,  $R^2$  in channels spaced by 1 MHz or less exhibits nonzero correlation. This type of behavior is as good as any spectral estimation can be without custom tuning for highly specific purposes.

[20] As an aside, note in Table 2 that there is an abrupt drop from approximately 0.7 or higher to approximately

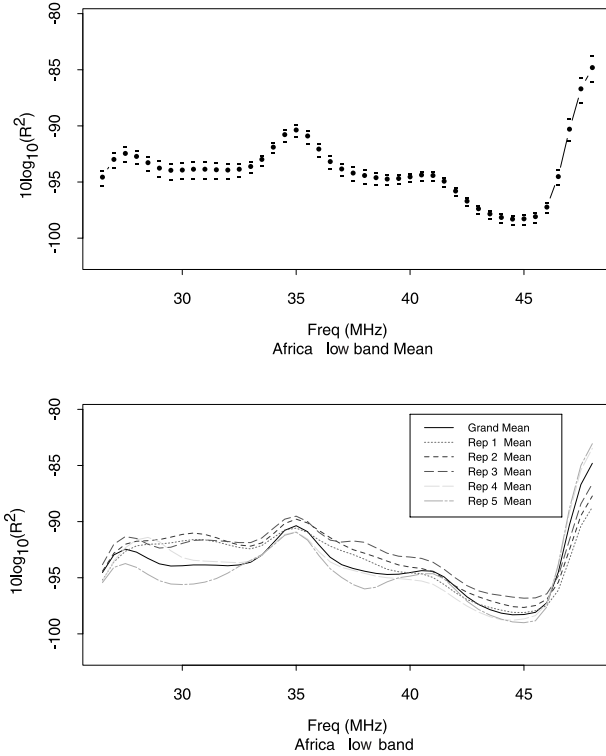


**Figure 2a.** (top) The average over all CV replicates of 40,000 10  $\mu$ s windows (overall mean) of  $10 \times \log_{10}(R^2)$  per 1 MHz wide subband and associated error bars. The error bars are at  $\bar{R}^2 \pm 2\hat{\sigma}_{\bar{R}^2}$  (displayed on decibel scale), where  $\hat{\sigma}_{\bar{R}^2}$  is the estimated standard deviation of  $R^2$  obtained from the variation of the means  $\bar{R}^2$  between replicates of 40,000 windows. (bottom) The overall mean as in the top panel and several of the CV replicate means.

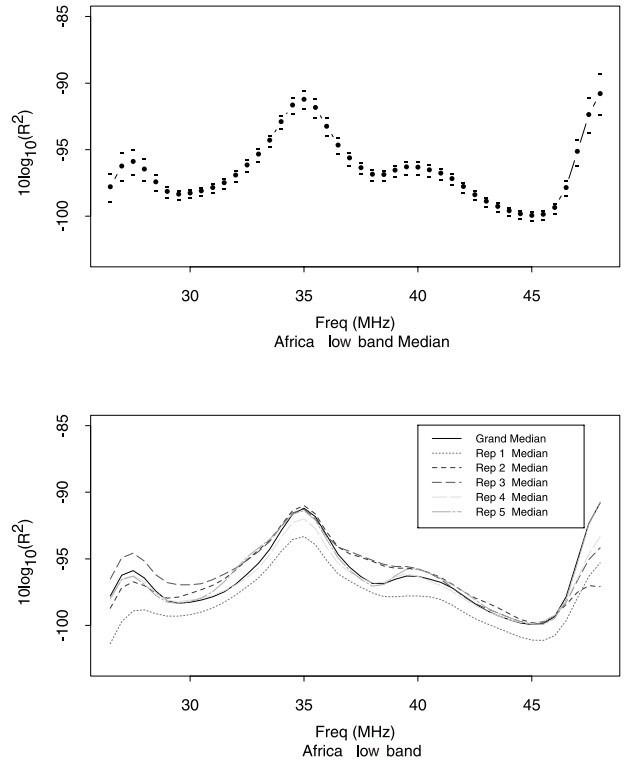


**Figure 2b.** Same as Figure 2a, except it is for the median.

0.3 in the last row. The last row is for the bin centered at 138.5 MHz, and we know of no reason for the abrupt drop. We investigated this behavior by examining the same correlation matrix for other regions and found that for some regions there was a gradual decrease toward 0 and for other regions; this same type of abrupt drop occurs at 138.5 MHz. For example, see Table 3, which is the same as Table 2 except the 40,000 randomly selected times are from Central America, and in this case there is no abrupt drop in the correlation values. We do not have an explanation for this behavior but recognize the value of further investigation. At present we simply provide the correlation matrix in Tables 2 and 3 as one feature of nonstationarity that has implications for multiband triggering schemes.

[21] Reasons for nonstationarity include sporadic man-made signals, and as mentioned above, the patch of Earth (each having differing amounts of industrial activity) within the FORTE view varies slowly and smoothly as FORTE transits its orbit. Either of these reasons can cause correlation of the type we observe in Tables 2 and 3.

[22] Additional evidence for nonstationarity includes: (1) confidence intervals for percentiles constructed from partitions of the 10  $\mu$ s windows do not overlap unless

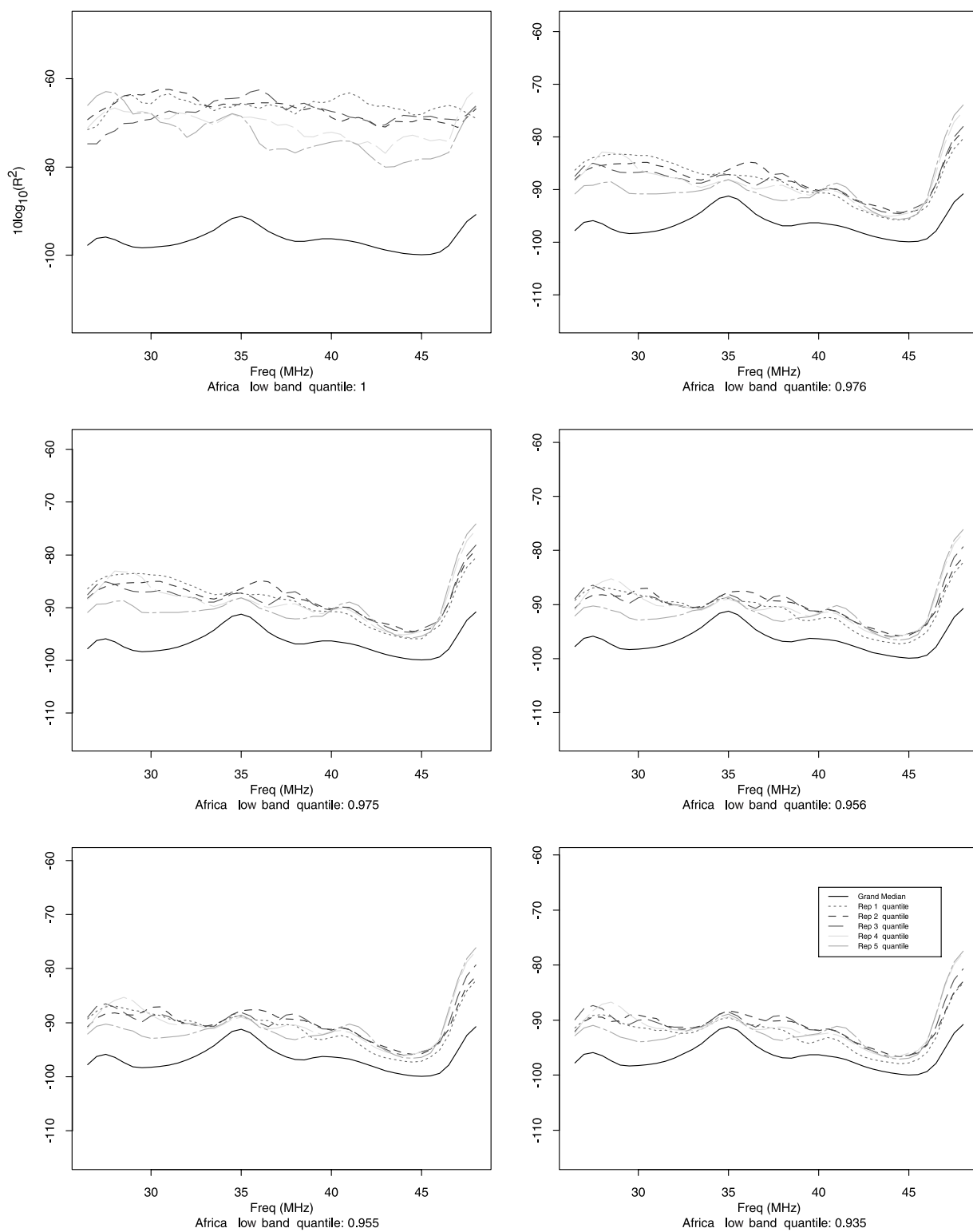


Figure 2c

wide time ranges (tens of days or more) are included in each partition, and (2) the standard deviation of the  $R^2$  at a given frequency is not well predicted from the within-partition standard deviation unless wide time ranges are included in each partition. The important observation that 10 or more days is necessary and sufficient in order for within-partition variation to predict between-partition variation suggests (empirically) that the variance as a function of time saturates after approximately several tens of days of separation between event records. We confirmed this by calculating the within-partition variance as a function of time range in the partition and observing this variance reach a saturation value after tens of days for each geographic region.

[23] Figure 1a gives informal evidence of nonstationarity for the Africa region (other regions also exhibit nonstationarity). The squared input data  $E^2$  in  $\text{V/m}^2$  (averaged over 500 points in each  $10\ \mu\text{s}$  window) for each of several passes is shown (a pass includes approximately 15 min of data). We extract approximately 20 or more signal-free  $10\ \mu\text{s}$  windows from each 409.6  $\mu\text{s}$  event record, and there are several event records per pass. For ease of viewing the data we then randomly select results from approximately 100 windows per pass. The time gaps between passes is tens of days (see legends). Clearly, the input data exhibit drifts (e.g., note the slow drift during the fifth pass) and spikes in amplitude. Figure 1b is the same type of plot, except we plot the squared amplitude  $R^2$  in a 1 MHz wide subband centered at 30 MHz. Figure 1c is the same as Figure 1b, except the center frequency is 40 MHz. From Figures 1a, 1b, and 1c, it is apparent that nonstationarity is due to both drifting over a time frame of minutes and spiking in the RF noise sources as observed from FORTE.

## 5.2. Cross Validation to Estimate Confidence Limits

[24] Because of this nonstationarity, we collected summary statistics from thousands of  $10\ \mu\text{s}$  time windows spanning the available time range from November 1997 to December 1999. We then randomly selected several (ten or more when possible) partitions from the entire available time range. Typically, each partition has 40,000  $10\ \mu\text{s}$  time windows and spans at least 100 days. This is a type of without-replacement CV. Each partition spans a wide time range, and for each partition, we calculate summary statistics to describe the distribution of  $R^2$  (such as the percentiles and the mean).

[25] If we force short time durations in each partition (such as a fraction of day), the observed variation among

summary statistics (such as the mean) between partitions is much larger than predicted on the basis of the within-partition variation. For example, in the SE Asia region we used partitions having 40,000  $10\ \mu\text{s}$  time windows but spaced in time to span only a fraction of a day. The standard deviation of the mean of  $R^2$  at a given frequency was approximately  $40,000^{1/2}$  times larger than expected under the assumption that the 40,000  $10\ \mu\text{s}$  time windows give independent estimates of the mean of  $R^2$ . This is due to nonstationarity that, by definition, implies that one small-time-range partition is likely to sample the noise during a low-value time period, and a second small-time-range partition is likely to sample the noise during a high-value time period.

[26] The partitioning scheme we use reduces the possibility of having artificially low variation within each partition because of the large time range included in each partition. We have empirically confirmed that the variation among the means of  $R^2$  across partitions at a given frequency agrees with the predicted variation provided the time range within each partition is large enough. For example, again using the SE Asia region, and forcing each partition to span 111 days or more (111 days was logistically convenient on the basis of how we collected the data and was adequately long), the observed standard deviation in  $R^2$  (in decibels) for the 8 frequency bins was 0.04, 0.05, 0.03, 0.03, 0.02, 0.02, 0.06, and 0.13. The predicted standard deviation (equal to the calculated standard deviation within each partition divided by the square root of the partition size of approximately 40,000) was 0.06, 0.05, 0.03, 0.04, 0.03, 0.05, and 0.11, which is in excellent agreement with the observed. To summarize these issues:

[27] 1. The time series of  $R^2$  at each frequency is nonstationary. Several stationarity tests have been firmly statistically rejected. The simplest such test is whether the within-partition variance predicts the between-partition variance regardless of the time range included in the partition. The result is that the time range included in each partition does matter up to a saturation that occurs after tens of days or more are included in each partition.

[28] 2. Ideally, each partition would span a wide enough time range that the within-partition variation of any summary statistic (such as the mean of  $R^2$ ) would accurately predict the between-partition variation. Fortunately, provided the time range between partitions spans a wide range, the between-partition variation can still be used to estimate confidence limits for estimated

**Figure 2c.** Quantiles of  $10 \times \log_{10}(R^2)$  averaged over each of several CV replicates and the overall median of  $10 \times \log_{10}(R^2)$ . The top row quantiles are chosen to give a 99% confidence interval (CI) for the 0.99 quantile. The middle row quantiles are chosen to give a 99% CI for the 0.97 quantile, and the bottom row quantiles are chosen to give a 99% CI for the 0.95 quantile. All figures display in the decibel scale.



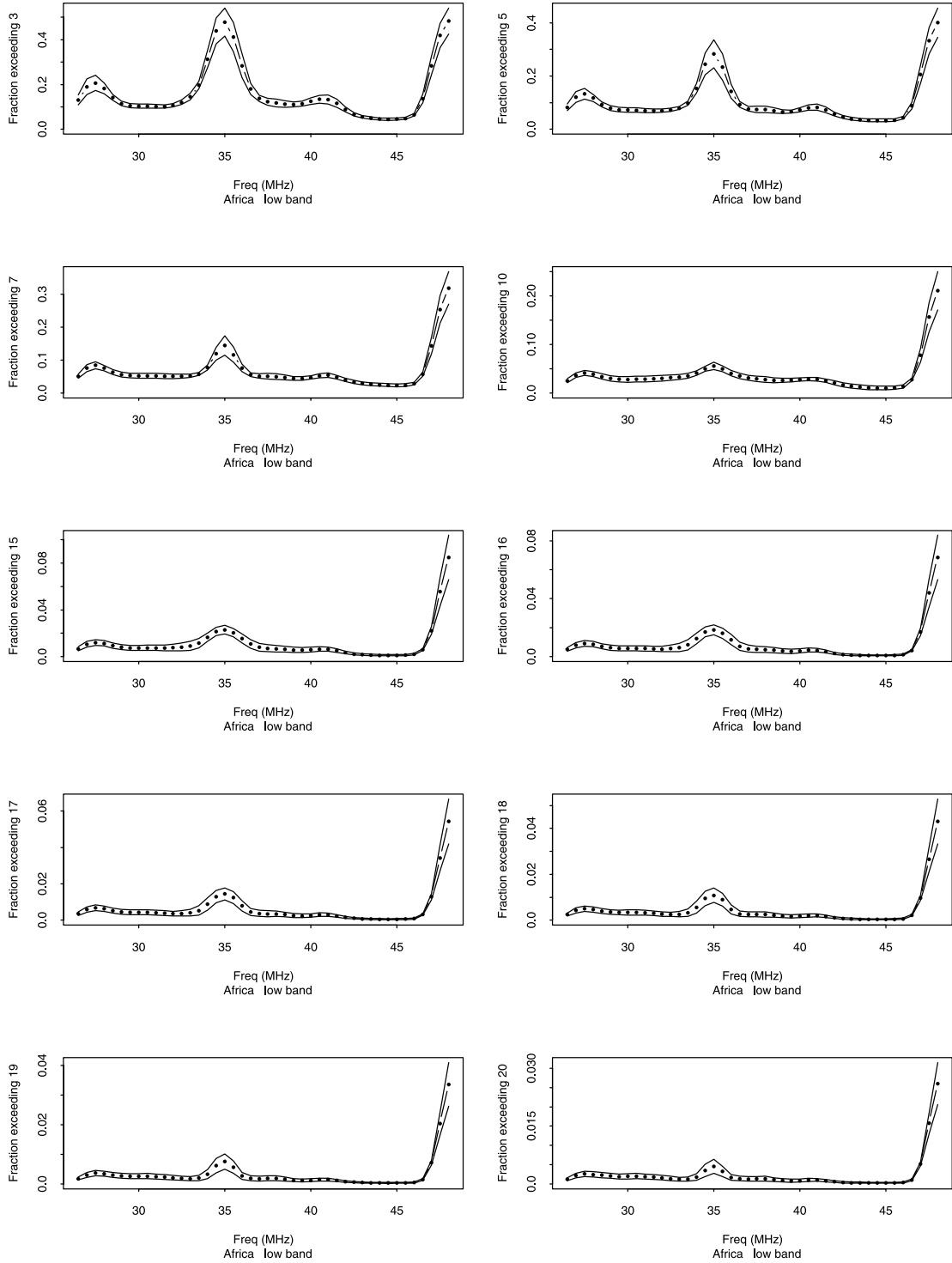


**Figure 2d.** The fraction exceeding the given threshold (3–20) is on the decibel scale, i.e., the fraction of  $10 \times \log_{10}(R^2)$  values per 1 MHz wide subband that exceed the given threshold.

parameters. Therefore, even if the within-partition variation is too small to accurately predict the between-partition variation, the between-partition variation can still be used to assign confidence limits to estimated parameters.

[29] 3. To estimate parameters such as the mean, median, or 99th percentile, we use a type of CV that requires the between-partition time ranges to be large (at least tens of days). Ideally, the within-partition time ranges are also large so that they predict the between-partition variation adequately. We then report the overall mean of the statistic that estimates the chosen parameter and the empirical standard deviation of the statistic between partitions as a measure of confidence in the estimated parameter.

[30] The central limit theorem (CLT) [Serfling, 1980] suggests that this overall mean is approximately Gaussian with a standard deviation approximately equal to the empirical standard deviation across partitions. We have made empirical tests of this claim for estimates of the mean and several percentiles, and in all cases the estimates are approximately Gaussian. Suppose the

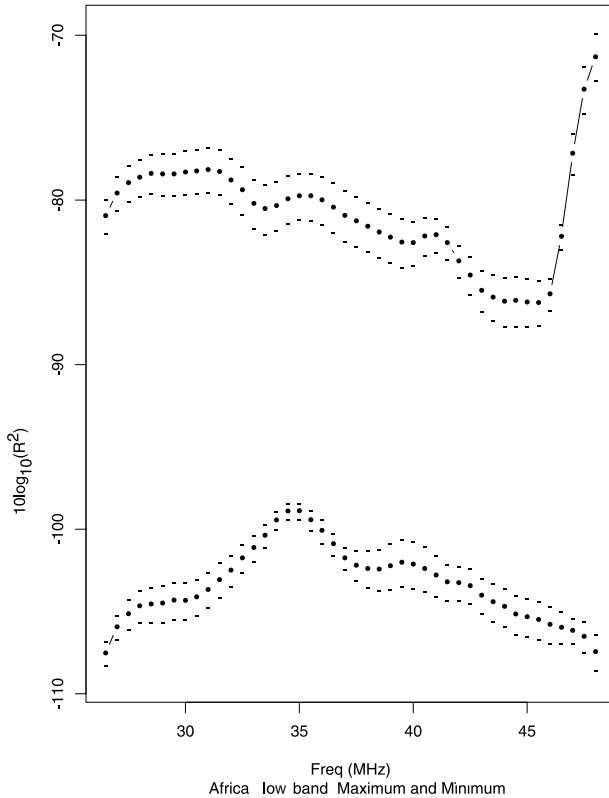


**Figure 2e.** Africa region: the average maximum and average minimum of  $10 \times \log_{10}(R^2)$  over all CV replicates and associated error bars.

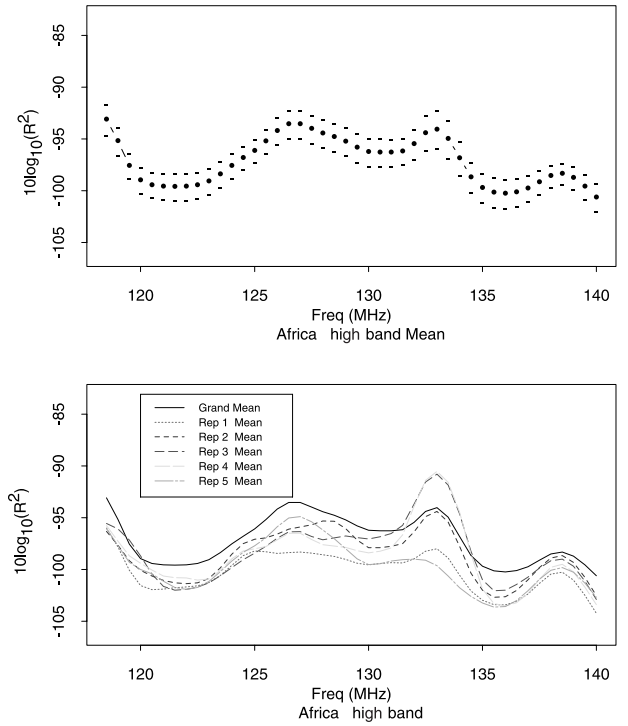


**Figure 2f.** (top) The average over all CV replicates of 40,000  $10 \mu/s$  windows (overall mean) of  $10 \times \log_{10}(R^2)$  per 1 MHz wide subband and associated error bars. The error bars are at  $\bar{R}^2 \pm 2\hat{\sigma}_{\bar{R}^2}$  (displayed on decibel scale), where  $\hat{\sigma}_{\bar{R}^2}$  is the estimated standard deviation of  $\bar{R}^2$  obtained from the variation of the means  $\bar{R}^2$  between replicates of 40,000 windows. (bottom) The overall mean as in the top panel and several of the CV replicate means.

smoothed power estimates were badly non-Gaussian and/or that estimates of percentiles were badly non-Gaussian. The CLT still applies (the quantity  $x$  can be highly non-Gaussian, but averages of 30 or more  $x$  values will still be nearly Gaussian under mild assumptions). The only concern here is to whether a sufficient time range between partitions is used, so that between-partition variation “saturates,” as discussed in issue (2) above. It is desired but not required that within-partition variation also saturate. That is, provided each partition spans enough days to explore the full noise distribution, the variability of the statistic across partitions is well estimated by the variability within the partition. This is a useful but not necessary feature that arises from using partitions that each span a large time range.

[31] One word of caution: the protocol for FORTE collection of TIPP events could, e.g., lead to long periods of sampling only from North Africa and not South Africa. Therefore we cannot be certain that the noise

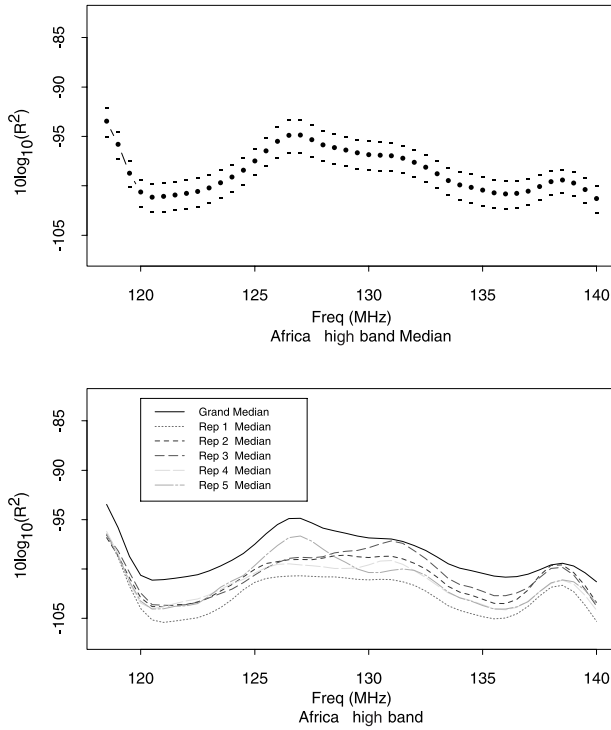


**Figure 2g.** Same as Figure 2f, except it is for the median.

summary for Africa is truly representative of all of Africa. This is an artifact of the FORTE collection protocol that is beyond our control and the CLT will not apply in this case.

### 5.3. Spectral Analysis Approach

[32] Let the electric field  $E_t$  at the satellite be denoted  $X_t$  and assume  $X_t = a_0 + \sum_{p=1}^{n/2-1} R_{p,t} \cos(\omega_{p,t}t + \phi_p) + e_t$ , where  $e_t$  is noise. Note that the amplitude  $R_{p,t}$  and frequency  $\omega_{p,t}$  are time-dependent, which is one way to express nonstationarity.

[33] For nonstationary time series, there are several reasonable ways to estimate the instantaneous value of  $R^2$  in each frequency [Bloomfield, 2000, chap. 7]. One of the simplest is to partition the time series into small time windows or segments and to compute the raw (unsmoothed) periodogram for each window. The raw periodogram is known to be excessively noisy (does not converge to the true value), so various smoothing

techniques have been developed to improve the quality of the estimate. Any smoothing method attempts to reduce variance at the expense of adding bias. If the variance reduction exceeds the bias, then the smoothing reduces the total error. We smooth the raw periodogram using a 1 MHz wide smoother (Appendix A).

[34] Bloomfield [2000] refers to methods for estimating “instantaneous” amplitude or phase as “complex demodulation.” Consider estimating  $R_{p,t}$  from nonstationary data. The simplest approach is to bin the time series into small time segments and estimate the squared amplitude for each spectral bin for each time segment. A similar approach [Fitzgerald, 2001] estimated the squared amplitude at each time point, but because of smoothing in the frequency domain with a 1 MHz wide bandwidth, the resulting time series of estimates was then resampled at a lower rate.

[35] Appendix A describes the well-known issues of resolution (bandwidth), stability (repeatability of amplitude estimates over segments of the time series), leakage (sidelobes in the spectral window imply that  $R^2$  at a given frequency will erroneously contribute to  $R^2$  at other frequencies unless steps are taken), and smoothness (similar to stability).

[36] The FORTE RF raw time series  $E$  (V/m) is recorded at  $20 \times 10^{-9}$  s intervals, and we desired a 2.5 MHz spectral resolution of noise-free signals after smoothing. Specifically, if a pure component signal at 30 MHz contributes to the estimate of  $R^2$  (due to the smoothing operation) at 28.5 MHz, that is acceptable. However, it is not acceptable for the 30 MHz signal to contribute to the estimate of  $R^2$  at 27.5 MHz or less or at 32.5 MHz or more. By choice of bandwidth we can achieve the 2.5 MHz resolution, and we empirically confirmed that the estimated  $R^2$  (the smoothed squared amplitude, see Appendix A) from simulated signals without noise with components spaced by 2.5 MHz or more were uncorrelated. Also, recall from the subsection regarding nonstationarity that observed correlations in sub-bands separated by 2.5 MHz or more (Tables 2 and 3) cannot be explained on the basis of our estimation scheme because the  $R^2$  estimates were based on a 1 MHz bandwidth smoother.

[37] Qualitatively, the product of the temporal and spectral resolution should be approximately 1–10, and  $10 \mu\text{s} \times 1 \text{ MHz} = 10$ . A reasonable time window is therefore approximately 200–1000 points, representing 5–20  $\mu\text{s}$  time segments. All results given here used 10  $\mu\text{s}$  time segments (500 points) and use the algorithm

**Figure 2h.** Quantiles of  $10 \times \log_{10}(R^2)$  averaged over each of several CV replicates and the overall median of  $10 \times \log_{10}(R^2)$ . The top row quantiles are chosen to give a 99% confidence interval (CI) for the 0.99 quantile. The middle row quantiles are chosen to give a 99% CI for the 0.97 quantile, and the bottom row quantiles are chosen to give a 99% CI for the 0.95 quantile. All figures display in the decibel scale.

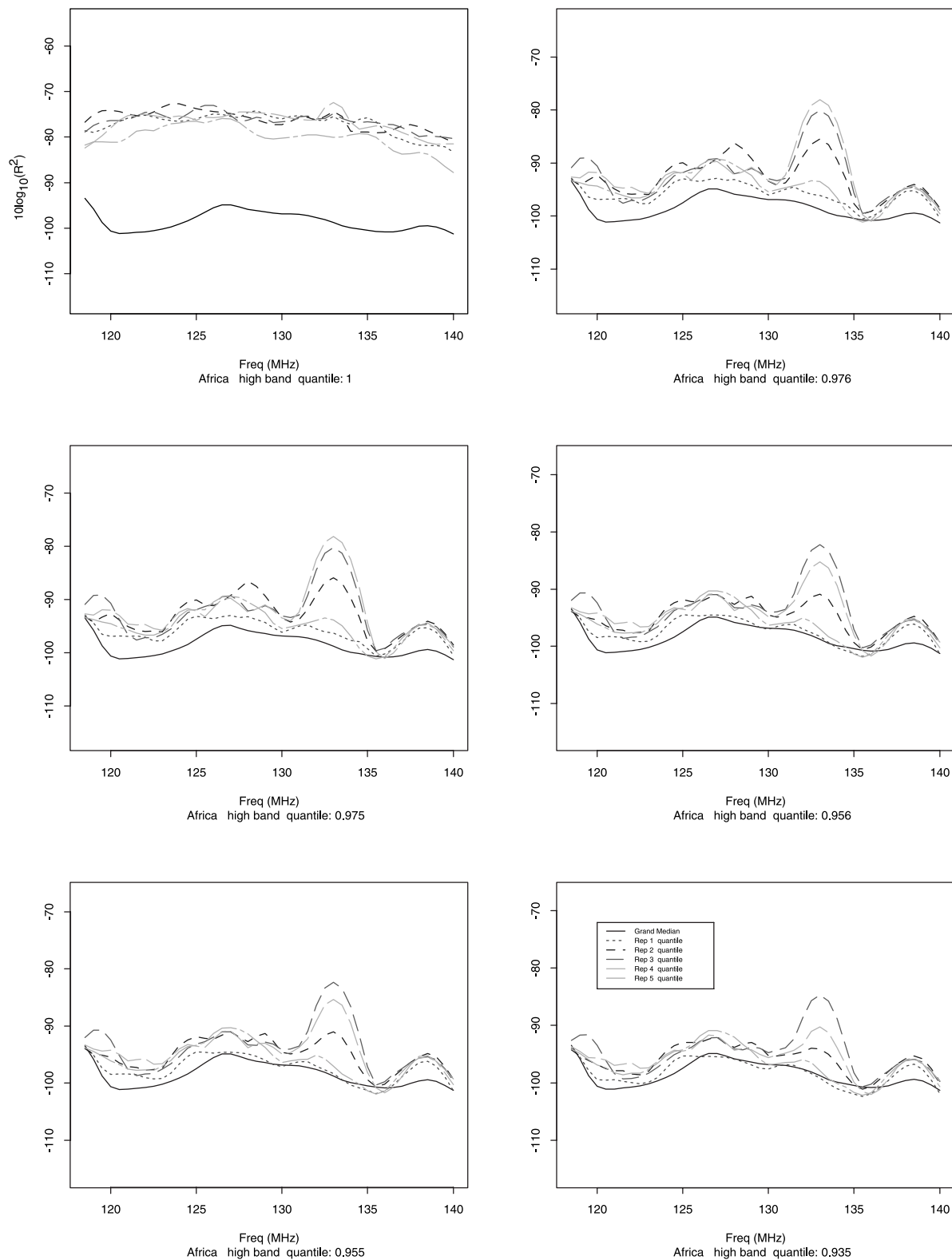
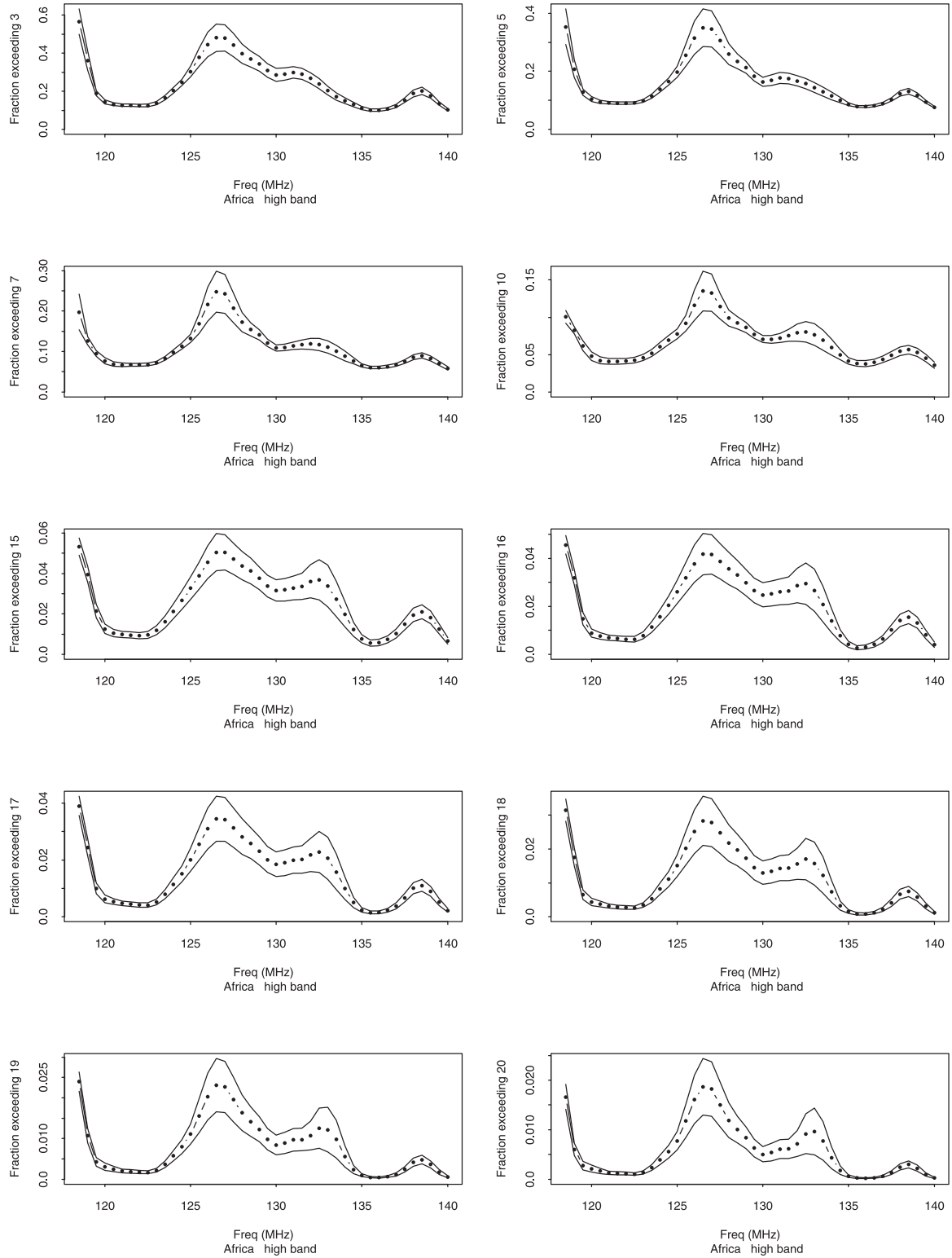


Figure 2h



**Figure 2i.** The fraction of  $10 \times \log_{10}(R^2)$  values per 1 MHz wide subband that exceed the given threshold.



given in Appendix A to compute the smoothed squared amplitude,  $R^2$ , at each center frequency in steps of 0.5 MHz.

#### 5.4. RF Noise Survey Summary

[38] We computed and archived estimates of  $R^2$  from each of 44 evenly spaced frequencies in 0.5 MHz steps from 26.5 to 48 MHz for the low band and from 118.5 to 144 MHz for the high band, from each full 10  $\mu$ s time segment, from each of the two “signal-free” time segments, and from each of many passes over each of 13 geographic regions.

[39] Graphical summary statistics are provided in Figures 2a–2j for the Africa region, and all involve the distribution of  $R^2$ . Unless stated otherwise, all figures convert to decibels and plot  $10 \times \log_{10}(R^2)$ . The typical magnitude of this noise is of interest because this is the noise that limits signal detection in triggered RF broadband signal recordings as mentioned in the Introduction. Therefore we present the following attributes: mean, median, upper percentiles, fraction that exceed potential trigger thresholds, as well as the maximum and mini-

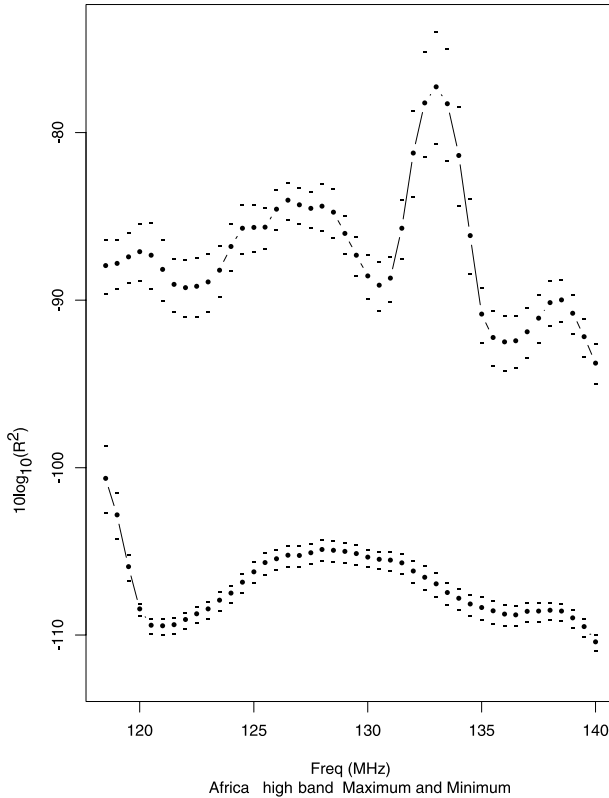


**Figure 2j.** The average maximum and average minimum of  $10 \times \log_{10}(R^2)$  over all CV replicates and associated error bars.

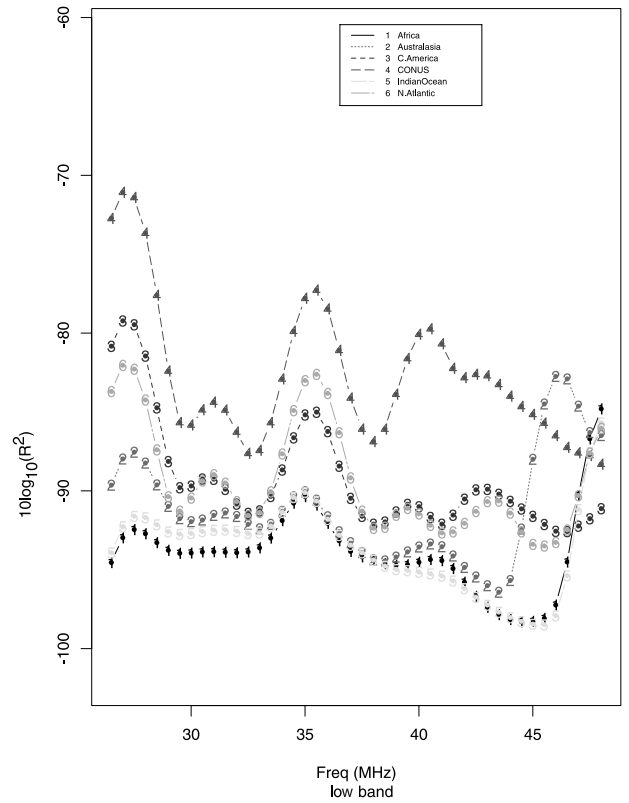


**Figure 3a.** The average of  $\log_{10}(R^2)$  values per 1 MHz wide subband (low band) for regions 1–6 of the 13 geographic regions.

mum. We also provide confidence limits. In hypothetical repeats of the sampling procedure, the attributes are highly likely (with approximately 95% probability) to lie within these limits.

[40] Figures 2a–2e are for the low band in Africa and include:

[41] 1. Figure 2a: An estimate of the overall mean of  $R^2$  and confidence limits. In all cases, the limits are at the estimate  $\pm$  twice the standard deviation of the estimate at each frequency (top of Figure 2a), including the means from several partitions (bottom of Figure 2a).

[42] 2. Figure 2b: Same as Figure 2a except it is for the median (top and bottom of Figure 2b).

[43] 3. Figure 2c: An estimate of six high percentiles of  $R^2$  and confidence limits of the estimate at each frequency, including the estimate from each of several partitions (Figure 2c). The three rows in Figure 2c each give percentiles in pairs that were chosen [Serfling, 1980] for bounding the 99th, 97th, and 95th percentiles with 99% probability.

[44] 4. Figure 2d: An estimate of the fraction of  $10 \times \log_{10}(R^2)$  that exceed the thresholds  $T = 3, 5, 7, 10, 15$ ,

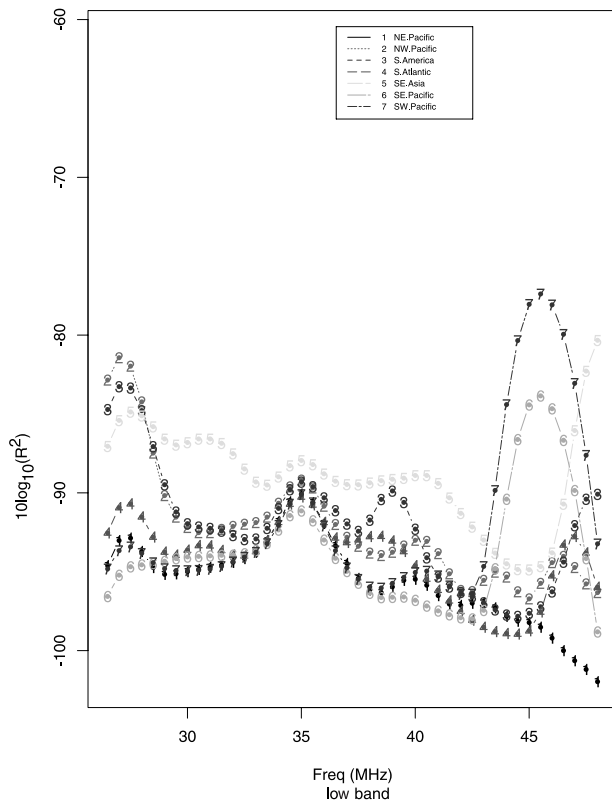


**Figure 3b.** The average of  $\log_{10}(R^2)$  values per 1 MHz wide subband (low band) for regions 7–13 of the 13 geographic regions.

16, 17, 18, 19, and 20, and the confidence limits at each frequency (Figure 2d).

[45] 5. Figure 2e: An estimate of the minimum and maximum of  $10 \times \log_{10}(R^2)$  and associated confidence limits (2e).

[46] Regarding Figure 2d, the FORTE trigger level was set at 14–20 dB above the noise [Lehtinen *et al.*, 2004], but because multiple bands must alarm during a coincidence time window, the alarm rate is very low on pure noise. This survey provides estimates of the per-channel alarm rates at candidate thresholds.

[47] Figures 2f–2j are the same except for the high band of Africa. We include them here as an example of the difference in noise magnitudes between the two bands. These same figures for the other 12 regions are available [Burr *et al.*, 2002].

[48] Here we include only Figures 3a–3h as a high-level summary of the 13 regions. Figure 3a is the overall mean for the low band for regions 1–6 (in alphabetical order). Figure 3b is the overall mean for the low band for regions 7–13 (the figure legend is from 1 to 7 to avoid double digits in the figure labels). Figures 3c and 3d are

the same as Figures 3a and 3b, respectively, except they are for the median. Figures 3e–3g are the same as Figures 3a–3d, respectively, except they are for the high band. We discuss features in these plots in the next section.

[49] Appendix B provides additional numerical summaries, and tabular summary data (such as percentiles which are useful for setting alarm thresholds) for each region for the low and high band for each of the 44 frequencies are available [Burr *et al.*, 2002] (at [nis-www.lanl.gov/nis-projects/forte\\_science](http://nis-www.lanl.gov/nis-projects/forte_science)).

## 6. Discussion

[50] Inspection of the plots for all 13 regions for the low band indicates the following qualitative information. All regions have peaks in the mean and median at approximately 28 and 35 MHz; some regions have peaks at approximately 48 MHz. Each region has its own characteristic spectrum, although some regions (such as Central America and North Atlantic) are very similar. The CONUS region has much higher (and in some cases

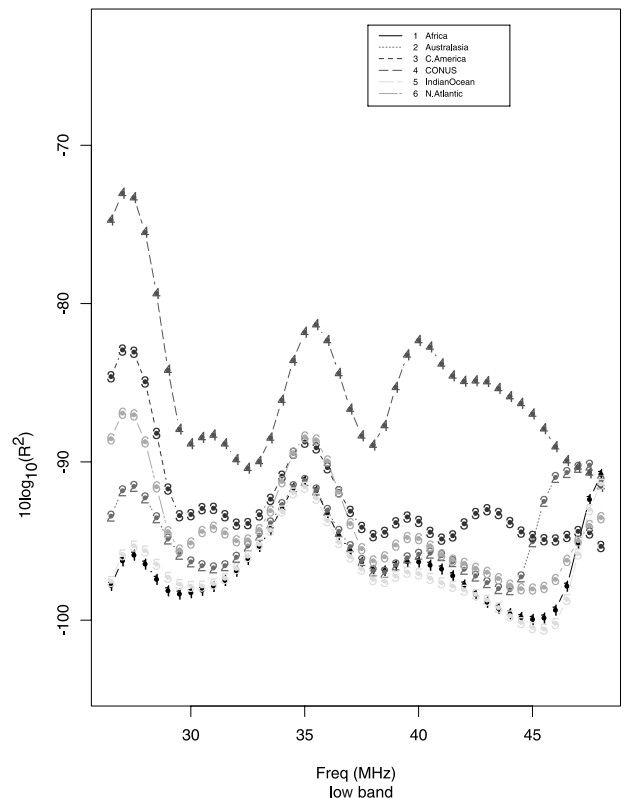


**Figure 3c.** The median of  $\log_{10}(R^2)$  values per 1 MHz wide subband (low band) for regions 1–6 of the 13 geographic regions.

sharper) peaks than other regions. The Africa and Indian Ocean regions are the quietest, except near 48 MHz. Australasia has a strong peak near 45 MHz, and CONUS has a strong peak near 40 MHz. SE Pacific and SW Pacific are also very similar, and both have large peaks at 45 MHz.

[51] Inspection of the plots for all 13 regions for the high band indicates the following qualitative information. The  $R^2$  versus frequency plot (for both the mean and median plots) is generally slightly smoother with less dramatic peaks than in the low band, except for a few strong peaks near 138 MHz (Australasia, Indian Ocean, South Atlantic, and SE Asia). All regions have some sort of broad and relatively flat peak spanning from 125 to 135 MHz. There is greater between-partition variability in the high-band data than in the low-band. The error bars are very large for the NE Pacific region, at least partly because there are only two partitions, each of only approximately 14,000 windows (rather than 40,000 windows; see Appendix B).

[52] The  $10 \times \log_{10}(R^2)$  values range from approximately  $-110$  to  $-70$  for both the low band and high

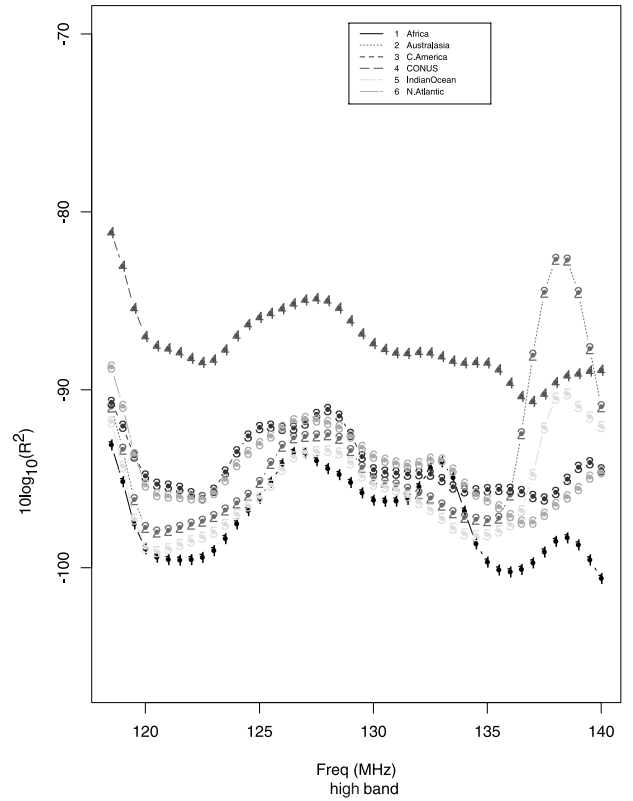


**Figure 3e.** The average of  $\log_{10}(R^2)$  values per 1 MHz wide subband (high band) for regions 1–6 of the 13 geographic regions.

band and are generally slightly larger in the low band. The CONUS region low band is notably higher, with values ranging from  $-105$  to  $-62$ .

[53] To check for trends, we compared the early period to the late period using  $t$  tests for means and medians (and other percentiles) and no statistically significant change over the review period of November 1997 to December 1999.

[54] In conclusion, we have provided a noise survey by region of RF noise as observed from the FORTE satellite at 800 km altitude. Numerical summaries in Appendix B supplement the graphical summaries provided here. Additional summary information is available at [nis-www.lanl.gov/nis-projects/forte\\_science](http://nis-www.lanl.gov/nis-projects/forte_science).

[55] For the purpose of setting alarm thresholds, a “static” threshold scheme can now be compared to a “dynamic” threshold scheme that frequently updates the background mean of  $R^2$  at each frequency by geographic region. For any of the alarm thresholds  $T$  considered here, and associated coincidence rule (such as the “5 of 8 channel within 162  $\mu$ s” rule that we described, tuned to alarm for a certain signal types), false alarm rates can be

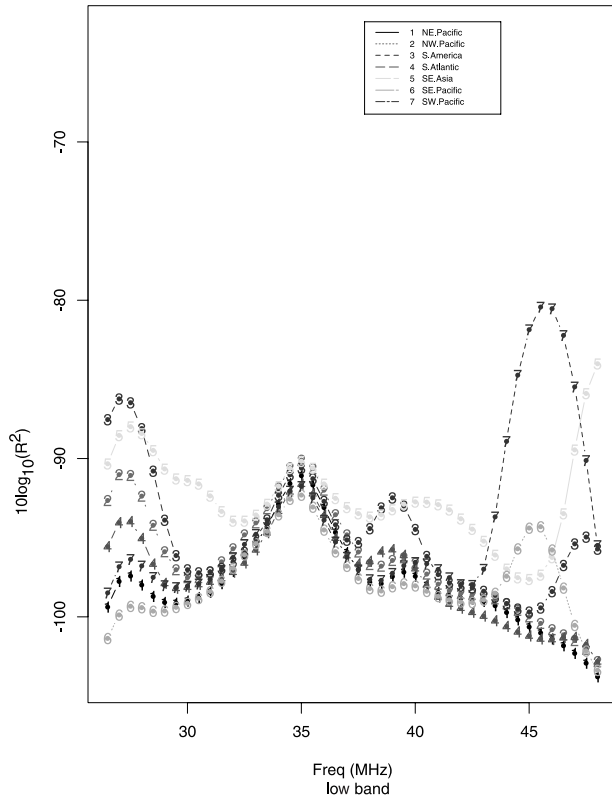


**Figure 3d.** The median of  $\log_{10}(R^2)$  values per 1 MHz wide subband (low band) for regions 7–13 of the 13 geographic regions.

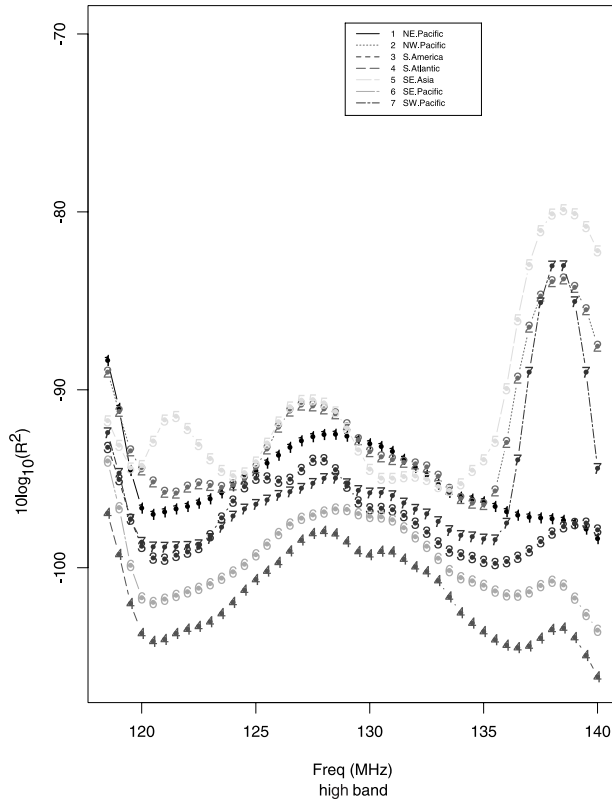


**Figure 3f.** The average of  $\log_{10}(R^2)$  values per 1 MHz wide subband (high band) for regions 7–13 of the 13 geographic regions.

calculated. If other thresholds are desired, interpolation is acceptable for thresholds within the 3–20 dB range presented here. For thresholds greater than 20 dB, extrapolation via model fitting is always dangerous, so if possible we recommend extending these results by reanalysis of the data.

## Appendix A: Spectral Analysis Methods

[56] The spectrum of a time series measures the probable amplitude of periodic components (as a function of frequency). It shifts emphasis away from searching for periodicities in a series toward the usually more informative evaluation of the relative amplitudes at all frequencies.

[57] *Bloomfield* [2000, chap. 7] refers to methods for estimating “instantaneous” amplitude or phase as “complex demodulation.” Consider estimating  $R_t$  from non-stationary data (let the electric field at the satellite  $E_t$  be denoted  $X_t$  here),  $X_t = R_t \cos(2\pi\omega_i T + \phi_t) + e_t$ , where  $e_t$  is noise (or more generally, from data that is a linear combination of many such time-dependent frequencies

$f_t$  and amplitudes  $R_t$ ). The simplest approach is to bin the time series into small time segments and estimate the squared amplitude  $R_t^2$  for each spectral bin for each time segment. Using a similar approach *Fitzgerald* [2001] estimated the  $R_t^2$  at each time point, but because of smoothing in the frequency domain with a 1 MHz bandwidth, the resulting time series of estimates was then resampled at a lower rate.

[58] Any sequence of  $n$  numbers (we assume  $n$  is even) has the Fourier series representation  $X_t = a_0 + \sum_{p=1}^{n/2-1} \{a_p \cos(2\pi p t/n) + b_p \sin(2\pi p t/n)\}$ , where the Fourier coefficients satisfy  $a_p(f) = 2/n \sum_{t=0}^{n-1} \{X_t \cos(2\pi p t/n)\}$  and  $b_p(f) = 2/n \sum_{t=0}^{n-1} X_t \sin(2\pi p t/n)$ ,  $a_0 = \bar{x}$  and  $a_{n/2} = \sum_{t=1}^n (-1)^t X_t/n$ . It follows (Parseval’s theorem) that  $\sum_{t=1}^n (X_t - \bar{X})^2/n = \sum_{p=1}^{n/2-1} \{R_p^2/2 + a_{n/2}^2\}$ , where  $R_p^2 = a_p^2 + b_p^2$  is the squared amplitude of the  $p^{\text{th}}$  harmonic, and a useful form for  $p \neq n/2$  is  $X_t = a_0 + \sum_{p=1}^{n/2-1} R_p \cos(\omega_p t + \phi_p)$  with the phase  $\phi_p = \tan^{-1}(-b_p/a_p)$ . Parseval’s theorem implies that the variance of the  $n$  observations can be decomposed into contributions from each of the harmonics. The plot of  $nR_p^2/(4\pi)$  versus  $\omega_p$  is usually called the periodogram, although other definitions have been used.

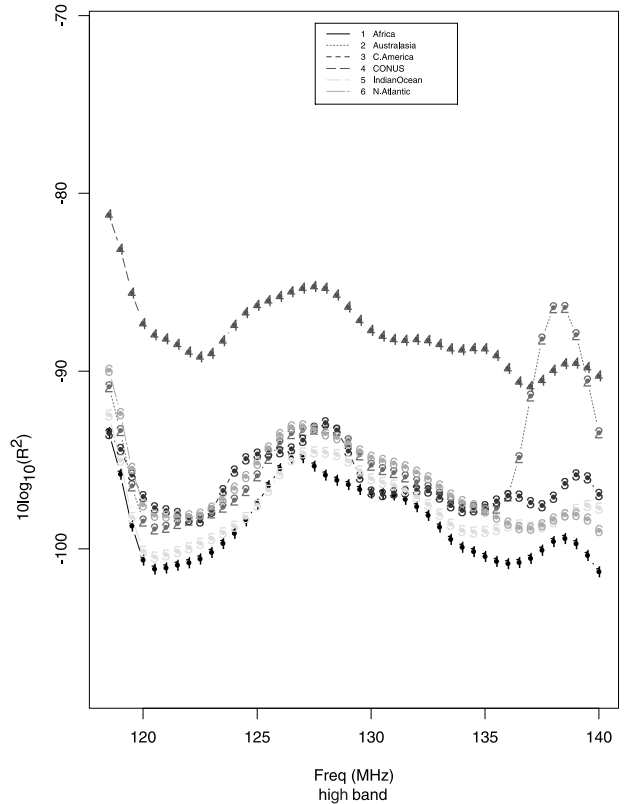


**Figure 3g.** The median of  $\log_{10}(R^2)$  values per 1 MHz wide subband (high band) for regions 1–6 of the 13 geographic regions.

[59] It is simple to show (using orthogonality of the sin and cosine functions) that if the sequence  $X_1, X_2, \dots, X_n$  is independent and identically distributed with the standard normal distribution, then the Fourier coefficients  $a_p$  and  $b_p$  each have an independent normal distribution with mean zero and variance  $2/n$ . It also follows that the estimated squared amplitude ( $R^2$ ) has a  $\chi^2_2$  distribution, with the scaling factor  $\sqrt{2/n}$  [Bloomfield, 2000, p. 90]. We usually plot the estimated  $R^2$  in decibels ( $10 \times \log_{10}(R^2)$ ), and the scaling factor does not impact the range in dB units.

[60] The  $\chi^2_2$  distribution is commonly called the Rayleigh distribution. Fitzgerald [2001] investigated the distribution of estimated  $R^2$  using LAPP-generated (Los Alamos Portable Pulsar) records and concluded that the Nakagami-Rice distribution provided a better fit than the Rayleigh. The explanation is that FORTE noise is better described by a random Gaussian process superimposed on narrow band transmissions, which is the classic motivation for the Nakagami-Rice distribution. Because the  $\chi^2_2$  distribution is highly variable, the estimated  $R^2$  is highly variable. Much literature has been

**Table 4.** Number of Partitions  $n$  of 40,000 10  $\mu$ s Windows by Region<sup>a</sup>

Region	$n$ for Low Band	$n$ for High Band
Africa	18	17
Australasia	15	16
Central America	15	16
CONUS	9	10
Indian Ocean	11	12
North Atlantic	14	12
NE Pacific	2	2
NW Pacific	5	4
South America	7	7
South Atlantic	2	2
Southeast Asia	9	10
SE Pacific	4	4
SW Pacific	4	4

<sup>a</sup>In a few cases the partition size is less than 40,000 10  $\mu$ s windows.

devoted to spectral analysis, including methods for smoothing the raw  $R^2$  estimates to reduce variability at the expense of introducing some bias. One goal is to reduce the total variation around the true value. In our case the time series is nonstationary, so the “true” value of the  $R^2$  varies over time. We have investigated various tapering and smoothing schemes, but for our purposes here it is fully adequate to use a simple defensible spectral analysis method for all 13 geographic regions. All of our presented results use a simple Gaussian-shaped 1 MHz wide smoother. As described in section 5.1, using simulated data, we ensured that subbands separated by 2.5 MHz or more are uncorrelated when the true input is stationary (unless the noise is too large in cases where the input includes a signal having one or more pure-component frequencies) and that a known signal amplitude at known frequency is recovered exactly (this is not true under all smoothing schemes due to leakage).

[61] Using the 1 MHz wide smoother, we estimated  $R^2$  at each center frequency using the fast Fourier transform with 1 MHz wide Gaussian smoothing [Splup6 for Linux, 1999]. We then coded those same smoothed cosine and sin transforms in Perl. Because our Splup implementation was too slow for this amount of data, we confirmed that the Perl and Splup implementations gave the same results for a few test cases and then used Perl for the large-scale problem.

## Appendix B: Numerical Summaries of the Noise Survey Results

[62] The number of partitions  $n$  into 40,000 10  $\mu$ s windows is given for each region in Table 4. In a few cases the partition size is less than 40,000 10  $\mu$ s windows. This is because we divided the collected event

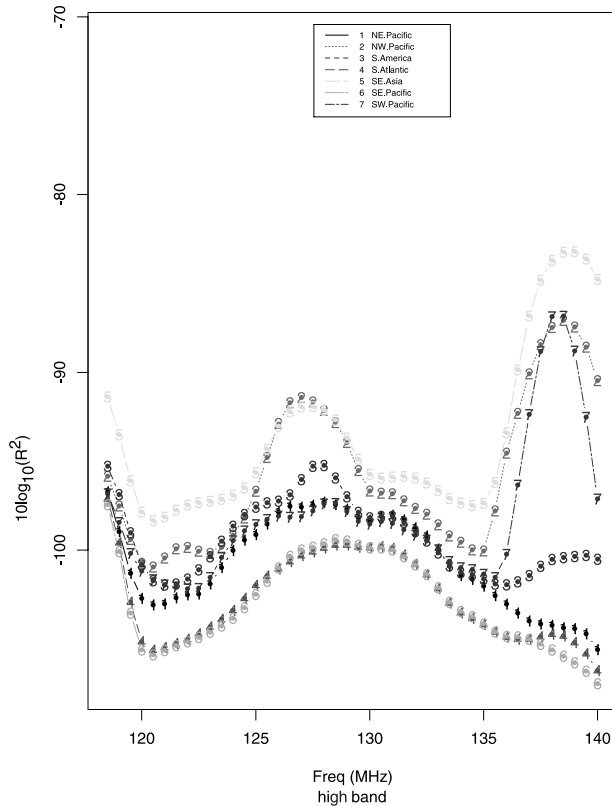


**Figure 3h.** The median of  $\log_{10}(R^2)$  values per 1 MHz wide subband (high band) for regions 7–13 of the 13 geographic regions.



records into two large groups, partitioned each large group into as many partitions having 40,000 windows as possible, and then used the remaining windows as a final smaller-sized partition. Therefore, for 2 of the partitions (the last partition in each of two large data collections) in each geographic region, there are fewer than 40,000 windows. Because of this, the South Atlantic and NE Pacific regions have the potential to exhibit larger variation among partitions than do the other regions (there are only two partitions for the low and high bands for both of these regions, and these each contain fewer than 40,000 windows). From the figures shown the NE Pacific region did exhibit more-than-typical variation among its two partitions (one with 12,445 windows and the other with 19,037 windows for the low band), but the South Atlantic region did not exhibit more-than-typical variation among its two partitions (one with 15,462 windows and the other with 14,457 windows for the low band). Approximately the same number of windows were available for the high band, with the same qualitative conclusions.

[63] **Acknowledgments.** We thank the reviewers, editor, and associate editor for their careful review of the manuscript. Their suggestions resulted in substantial improvements.

## References

- Bloomfield, P. (2000), *Fourier Analysis of Time Series: An Introduction*, 2nd ed., John Wiley, Hoboken, N. J.
- Burr, T., A. R. Jacobson, and A. Mielke (2002), A global radio frequency noise survey as observed by the FORTE satellite at 800-km altitude, *Internal Rep. LA-UR-02-6451*, Los Alamos Natl. Lab., Los Alamos, N. M.
- Fitzgerald, T. J. (2001), Statistics of FORTE noise between 29 and 47 MHz, *Internal Rep. LAUR-01-3095*, Los Alamos Natl. Lab., Los Alamos, N. M.
- Herman, J. R., J. A. Caruso, and R. G. Stone (1973), Radio astronomy explorer (RAE), I, Observations of terrestrial radio noise, *Planet. Space Sci.*, 21, 443–461.
- Jacobson, A. R. (2003), Relationship of intracloud-lightning radio-frequency power to lightning-storm height, as observed by the FORTE satellite, *J. Geophys. Res.*, 108(D7), 4204, doi:10.1029/2002JD002956.
- Jacobson, A. R., and T. E. L. Light (2003), Bimodal radiofrequency pulse distribution of intracloud-lightning signals recorded by the FORTE satellite, *J. Geophys. Res.*, 108(D9), 4266, doi:10.1029/2002JD002613.
- Jacobson, A. R., S. O. Knox, R. Franz, and D. C. Enemark (1999), FORTE observations of lightning radio-frequency signatures: Capabilities and basic results, *Radio Sci.*, 34(2), 337–354.
- Kaiser, M., M. Desch, J. Bougeret, R. Manning, and C. Meete (1996), Wind/WAVES observations of man-made radio transmissions, *Geophys. Res. Lett.*, 23(10), 1287–1290.
- LaBelle, J., R. Treumann, M. Boehm, and K. Gewecke (1989), Natural and man-made emissions at 1.0–5.6 MHz measured between 10 and 18 R<sub>E</sub>, *Radio Sci.*, 24(6), 725–737.
- Lehtinen, N. G., P. W. Gorham, A. R. Jacobson, and R. A. Roussel-Dupre (2004), FORTE satellite constraints on ultrahigh energy cosmic particle fluxes, *Phys. Rev. D*, 69, 1–14.
- Light, T. E. L., and A. R. Jacobson (2002), Characteristics of impulsive VHF lightning signals observed by the FORTE satellite, *J. Geophys. Res.*, 107(D24), 4756, doi:10.1029/2001JD001585.
- Serfling, R. (1980), *Approximation Theorems of Mathematical Statistics*, John Wiley, Hoboken, N. J.
- Spluse6 for Linux (1999), Insightful Corp., Seattle, Wash.
- Tierney, H. E., A. R. Jacobson, R. Roussel-Dupre, and W. H. Beasley (2002), Transionospheric pulse pairs originating in maritime, continental, and coastal thunderstorms: Pulse energy ratios, *Radio Sci.*, 37(3), 1039, doi:10.1029/2001RS002506.
- Volland, H. (1995), *Handbook of Atmospheric Electrodynamics*, CRC Press, Boca Raton, Fla.

T. Burr, Los Alamos National Laboratory, Mail Stop F600, Los Alamos, NM 87545, USA. (tburr@lanl.gov)

A. Jacobson, Los Alamos National Laboratory, Mail Stop D436, Los Alamos, NM 87545, USA.

A. Mielke, Los Alamos National Laboratory, Mail Stop D440, Los Alamos, NM 87545, USA.